Transport in Porous Media manuscript No.
(will be inserted by the editor)

Effective Rheology of Two-phase Flow in Three-Dimensional Porous Media: Experiment and Simulation

Santanu Sinha · Andrew T. Bender · Matthew Danczyk · Kayla Keepseagle · Cody A. Prather · Joshua M. Bray · Linn W. Thrane · Joseph D Seymour · Sarah L Codd · Alex Hansen

arXiv:1612.06101v1 [physics.flu-dyn] 19 Dec 2016

Received: date / Accepted: date

Abstract We present an experimental and numerical study of immiscible two-phase flow in 3-dimensional (3D) porous media to find the relationship between the volumetric flow rate (Q) and the total pressure difference (ΔP) in the steady state. We show that in the regime where capillary forces compete with the viscous forces, the distribution of capillary barriers at the interfaces effectively creates a yield threshold, making the fluids reminiscent of a Bingham viscoplastic fluid in the porous medium, introducing a threshold pressure P_t. In this regime, Q depends quadratically on an excess pressure drop ($\Delta P - P_t$). While increasing the flow-rate, there is a transition, beyond which the flow is Newtonian and the relationship is linear. In our experiments, we build a model porous medium using a column of glass beads transporting two fluids – de-ionized water and air. For the numerical study, reconstructed 3D pore-networks from real core samples are considered and the transport of wetting and non-wetting fluids through the network are modeled by tracking the fluid interfaces with time. We find agreement between our numerical and experimental results. Our results match the mean-field results reported earlier.

Keywords dynamical pore network model, reconstructed porous media, two-phase flow experiment, steady-state two-phase flow

Santanu Sinha
Beijing Computational Science Research Center, 10 East Xibeiwang Road, Haidian District, Beijing 100193, China.
E-mail: santanu@csrc.ac.cn

Alex Hansen
Beijing Computational Science Research Center, 10 East Xibeiwang Road, Haidian District, Beijing 100193, China.
Department of Physics, Norwegian University of Science and Technology, NTNU, N-7491 Trondheim, Norway.
E-mail: alex.hansen@ntnu.no

Andrew T. Bender · Matthew Danczyk · Kayla Keepseagle · Cody A. Prather · Joshua M. Bray · Linn W. Thrane · Sarah L Codd
Department of Mechanical and Industrial Engineering, Montana State University, Bozeman, MT, USA.
E-mail: scodd@montana.edu

Joseph D Seymour
Department of Chemical and Biological Engineering, Montana State University, Bozeman, MT, USA.
E-mail: jseymour@montana.edu

1 Introduction

The simultaneous flow of two immiscible fluids in porous media, otherwise known as two-phase flow [1,2], is getting increasing attention of both the scientific and industrial communities. These flows are encountered in many industrial and geophysical applications, such as carbon sequestration and oil recovery, groundwater management, blood flow in capillary vessels, catalyst supports used in automotive industry, bubble generation in microfluidics and many more. Extensive study of hydrodynamics in porous media is crucial for the development of these applied processes. While single-phase flows have been well characterized, many phenomena of steady-state immiscible two-phase flows in porous media are still not adequately understood.

In single-phase flow, the macro-scale pressure gradient (ΔP) over a porous medium scales linearly with the superficial fluid velocity governed by Darcy's law [3,4]. This is also true in the case of two-phase flows at high fluid velocities when capillary forces are negligible. However, at slow velocities when the capillary forces are comparable with the viscous forces, the total pressure gradient in the steady state does not scale linearly with the flow rate. In a fundamental experiment of two-phase flow of air and water-glycerol mixture in a two-dimensional (2D) model porous media made of glass beads in Hele-Shaw cell [5,6], it was observed that ΔP scales with the flow rate by a power law with an exponent 0.54. In a different experiment of two-phase flow in a three-dimensional (3D) porous medium, similar power law scaling between Q and ΔP was observed, but the exponents were found to vary in the range between 0.45 to 0.3 depending on the saturation [7].

This question about the non-linear relationship between ΔP and Q in steady-state two-phase flow of immiscible Newtonian fluid was addressed in detail by Sinha *et al.* [8,9]. It was shown that the capillary barriers at the interfaces between the fluids effectively create an effective yield threshold, making the fluids reminiscent of a Bingham viscoplastic fluid in the porous medium introducing an overall threshold pressure P_t in the system. A generalized Darcy equation was then obtained with mean-field calculations, where Q depends quadratically on an excess pressure drop ($\Delta P - P_t$) for low capillary numbers (Ca). The capillary number is a dimensionless number which describes different regimes of flow, defined as the ratio of the viscous to the capillary forces at the pore level given by $\mathrm{Ca} = \mu v/\gamma$. Here μ is the effective viscosity of the system, γ is the surface tension and v is the fluid velocity which is equal to the flow rate per cross-sectional pore area. When other parameters are constant, Ca will therefore be proportional to the flow rate, Q.

For a single capillary tube with a narrow pore-throat, there will be no flow through it as long as the pressure drop (Δp) across the tube is less than the capillary barrier (p_t). Above the threshold pressure, the average flow rate $\langle q \rangle$ through one tube can be obtained for the steady-state conditions by integrating the instantaneous linear two-phase flow equation over the whole tube. The problem becomes equivalent to a forced over-damped oscillator, providing a threshold pressure followed by a square-root singularity given by [9],

$$\langle q \rangle = -\sigma_0 \ \mathrm{sgn}(\Delta p) \begin{cases} \sqrt{\Delta p^2 - p_t^2} & \text{if } |\Delta p| > p_t \ , \\ 0 & \text{if } |\Delta p| \leq p_t \ , \end{cases} \tag{1}$$

where sgn() is the sign function and σ_0 contains the terms related to permeability. Close to the threshold, when $|\Delta p| \ll p_t$, the average flow $\langle q \rangle \sim \sqrt{|\Delta p| - p_t}$. This relationship leads to the non-linear conductivity of a single capillary given by $\sigma(\Delta p) = -\,\mathrm{d}q/\,\mathrm{d}(\Delta p)$ in the steady-state.[1] Using this expression of $\sigma(\Delta p)$ for each link, a mean-field theory was developed to find the relationship of the total flow rate for a homogeneous disordered network [8]. For a spatially uncorrelated distribution of threshold pressures, one obtains

$$Q = -C \frac{A}{L} \frac{K(S_{\mathrm{nw}})}{\mu(S_{\mathrm{nw}})} \mathrm{sgn}\,(\Delta P) \begin{cases} \left(|\Delta P| - P_t(S_{\mathrm{nw}})\right)^2 & \text{if } |\Delta P| > P_t \ , \\ 0 & \text{if } |\Delta P| \leq P_t \ , \end{cases} \tag{2}$$

[1] Steady state signifies that the macroscopic parameters describing the flow remain constant. It does *not* imply that the interfaces in the pores do not move, split or merge.

where L is length of the network, C is a constant with units of inverse pressure and $K(S_{\rm nw})$ is the effective permeability as a function of the non-wetting fluid saturation $S_{\rm nw}$. μ is the effective viscosity of the system given by $\mu = \mu_{\rm nw}S_{\rm nw} + \mu_{\rm w}(1-S_{\rm nw})$ where $\mu_{\rm w}$ and $\mu_{\rm nw}$ are the viscosities of the wetting and the non-wetting fluids respectively. For the high flow rates, there is a transition, beyond which the two-phase flow rate varies linearly with the total pressure drop. This quadratic relationship between Q and the excess pressure drop $(\Delta P - P_t)$ at low Ca and the crossover to the Newtonian flow regime at high Ca were also verified with extensive numerical simulations. However, the simulations were performed only for regular 2D networks of disordered tubes and not for 3D pore networks.

This situation of two-phase flow of two immiscible Newtonian fluids in a disordered network is similar to the flow of a Bingham viscoplastic fluid in a disorder network [10,11]. For a Bingham fluid inside a uniform tube, no fluid flows as long as the pressure across the tube is less than a threshold value and the flow is linear above the threshold. There are more complicated non-trivial flow regimes that exist for Bingham fluid flowing through a rough channel depending on the roughness [12]. When a Bingham fluid flows through a network of uniform tubes with a distribution of disorder in the thresholds, it was shown that there is an overall threshold pressure (P_t) for the whole network. The threshold pressure along one continuous flow-path throughout the entire system is the sum of all the thresholds along that path and the minimum sum along all such possible paths corresponds to the threshold pressure P_t for the entire system. The fluid starts flowing beyond P_t and any further increase in the pressure difference across the network by a value $\mathrm{d}P$ will cause an increase in the number of conducting links $\mathrm{d}N$ in the network. With a reasonably smooth distribution of thresholds, we can consider $\mathrm{d}N \propto \mathrm{d}P$ and the change in the conductance Σ of the network can then be written as $\mathrm{d}\Sigma \propto \mathrm{d}N \propto \mathrm{d}P$. The increase in the flow rate $\mathrm{d}Q \propto \Sigma\,\mathrm{d}P$, and integration over these will lead to the same quadratic relationship shown in equation 2 [10]. When all the links are conducting beyond a certain pressure drop, Σ becomes constant and then there is the crossover where Q becomes linear with P. Notice that, the flow-rate through one link above the threshold pressure varies linearly with the excess pressure drop for a Bingham fluid whereas in two-phase flow through a single varying-diameter capillary it is non-linear, but still the two phase flow in a disorder network effectively behaves similar to a Bingham viscoplastic fluid in the steady state.

The experiments on two-phase flow [5,6,7] have shown this non-linear quadratic dependence between flow rate and pressure drop but the existence of the threshold pressure was not investigated in any experiment. In support of the experimental results observed in the 2D experiment, a scaling theory was proposed in [6] showing $Q \sim \Delta P^2$ without considering a threshold pressure drop. The scaling theory was based on the assumption that the fluids flow through different channels and there are stuck clusters in between them. The scaling theory is as follows. Let us consider a 2D porous media of width W and length L where the overall pressure drop as well as the total flow is in the direction of length L. There is a number of flow channels n_l in the direction of overall flow. A characteristic length-scale l in between the channels is considered and therefore $n_l = W/l$. The flow through each channel is then, $q_c = ka^2\Delta P/(\mu L)$, where a is the cross section of one channel and k is the permeability of a channel. The total flow through all the channels is then $Q = n_l q_c = ka^2 W\Delta P/(\mu l L)$. In order to find the dependence of l on ΔP, it is assumed that the stuck clusters in between the channels are held in place by capillary forces p_c. If λ is the diameter of such a cluster, then the viscous pressure drop around it will be $\lambda\Delta P/L$, which should be $\leq p_c$ in order for the cluster to be held in place. Considering $\lambda\Delta P/L = p_c$ for the largest cluster which is not moving and assuming that the separation of the channels, l, is the same as the largest non-moving cluster diameter, i.e., $l \approx \lambda = p_c L/\Delta P$, one finds $Q = ka^2 W\Delta P^2/(\mu L^2 p_c)$ or $Q \sim \Delta P^2$. Though this scaling theory shows the quadratic dependence of Q on ΔP, it does not contain any threshold pressure. Moreover, if we extend this theory in 3 dimensions, the number of channels n_l should be equal to W^2/l^2 and following the same arguments we will find $Q \sim \Delta P^3$ for 3D. This is contradictory to the mean field theory [8], according to which the quadratic relationship does not depend of the dimensionality of the network. Secondly, the 3D experiments reported in Ref [7] showed that, without considering the threshold pressure, the log-log plot of Q and ΔP shows a variation in the slope in the range 0.45 to 0.3. Those experiments were performed for a

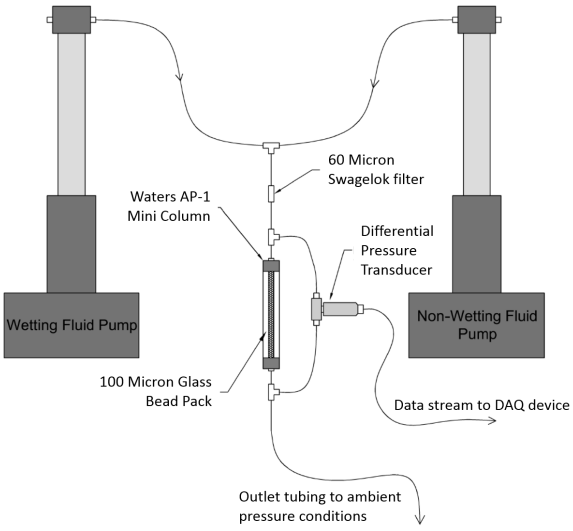

Fig. 1: The experimental setup of two-phase flow of deionized water as the wetting fluid and air as the non-wetting fluid through the column of borosilicate glass beads.

short range of capillary numbers and were difficult to draw any definitive conclusions from. It is therefore very important to perform extensive experiments and numerical simulations of two-phase flow in 3D porous medium to find the exact non-linear dependence of Q and ΔP and to check whether the scaling exponent varies with dimensionality of the system.

To our knowledge there is very little experimental work exploring these flows using a three-dimensional pore network. In this article, we present an extensive experimental and numerical study of the steady-state two-phase flow of immiscible Newtonian fluids. In the following, first we will present the experimental study of steady-state two-phase flow of air and deionized water. This work utilizes a three-dimensional porous medium, resulting in a more chaotic flow and increased fluctuations around a mean value. Significant work was done to collect high fidelity data and to accurately obtain the average differential pressures in the steady-state. We will then present our numerical work, describing the network model of two-phase flow in three dimensional reconstructed pore networks. From our experimental and computational results, we will show that there exists a global threshold pressure P_t, below which there is no flow through the system. The results are highly significant in understanding the non-Newtonian two-phase flow behavior of Newtonian fluids due to the dominant capillary forces in a disordered system.

2 Experimental Setup

Experiments were performed on a three-dimensional porous medium confined in a vertical column. The porous medium was comprised of randomly distributed borosilicate glass beads with diameter $d = 98 \pm 8\mu$m and porosity $\phi = 0.44$ (Cospheric LLC, Santa Barbara, CA). These micro-spheres were wet-filled and well packed into a Waters AP-1 Mini Chromatography Column with inner diameter $D = 5$mm and length $L = 70$mm. Filters at the inlet and outlet of the column consisted of a bed of glass microfibers and fine plastic mesh. The mesh allowed for uninhibited fluid flow, yet prevented the loss of glass beads. The filters aided in mixing the fluids to further homogenize the two phases before entering the porous media. This was done to emulate the alternating inlet boundary conditions as used in other experiments [6] or simulations

[8] and to minimize the slug-like flow of alternating fluids. The two immiscible fluids used in this study were deionized water as the wetting fluid, and air as the non-wetting fluid, having respective dynamic viscosities $\mu_{\mathrm{w}} = 1.002$Pa.s and $\mu_{\mathrm{nw}} = 1.84 \times 10^{-5}$Pa.s. This provides the viscosity ratio $M = \mu_{\mathrm{nw}}/\mu_{\mathrm{w}}$ equal to 1.8363×10^{-5}. The air-water surface tension at room temperature is around 0.073 N/m. The bond number comparing gravitational effects to the surface tension, $E_o = \Delta\rho g d^2/\gamma$ where $\Delta\rho$ is the difference in density of the fluids and g the gravitational acceleration, is around 0.001. If we assume the size of an air bubble in the system is of the order of the column diameter $D = 5$ mm, the ratio between the buoyancy and the capillary force is $(D/d)E_0 \approx 0.05$ making it possible to ignore gravitation in the analysis.

Two Teledyne Isco Model 500D syringe pumps were used to control the bulk flow rates of each respective fluid, which were then combined in a junction just above the column inlet. Polyetheretherketone (PEEK) tubing (Sigma-Aldrich Co.) and stainless steel fittings (Swagelok) comprised the flow system, and a sintered stainless steel 60µm filter element was used before the inlet to collect any small particulates in the inlet fluids and homogenize the phases. An Omega PX409 differential pressure transducer measured the pressure gradient over the column of glass micro-spheres. Pressure data was acquired using National Instruments LabVIEW at a sampling rate of 1000 samples per second, although sample compression was used to average 1000 samples into one data point, yielding one binned data point per second. A schematic of the experimental setup can be seen in Figure 1.

3 Experimental Results and Discussions

Our experimental study is focused on measuring the scaling coefficient α related to the scaling of the flow rate and the excess pressure drop, $(\Delta P - P_t) \sim \mathrm{Ca}^{\alpha}$, which has been shown to be independent of fractional flow, saturation and viscosity ratio [6,8]. Our experiments use non-wetting fractional flow $F_{\mathrm{nw}} = 0.5$ allowing for the volume of both syringe pumps to be fully utilized. All experimental parameters were kept constant except the flow rates of the fluids, so the overall bulk flow rate was varied initially in order to reach the desired capillary number. This paper focuses on experiments carried out at capillary numbers 10^{-4} to $10^{-5.4}$. Before each experiment, the bead pack was initially saturated with water (no air flow) which provided consistency between experiments. The experiments were conducted by simultaneously starting the flow of both water and air at the same flow rate, resulting in the desired non-wetting fractional flow of $F_{\mathrm{w}} = 0.5$. The total flow rate Q for any given capillary number Ca is obtained from the fluid velocity v given by $v = \gamma\mathrm{Ca}/\mu$, and then multiplying it with the effective cross-section A, $Q = Av$. Here μ is the effective viscosity at room temperature. The effective cross-sectional area A is obtained from the total cross-sectional area of the bead pack multiplied with its porosity ($\phi = 0.44$). The volumetric flow rate for each fluid (air and water) is then half of the calculated total flow rate Q. Due to the compressibility of the air, the phases likely competed at the junction, causing some degree alternating injections of water and air. Again, the filter was utilized as a means to reduce this phenomenon and create a more homogenized flow into the bead pack. The non-wetting saturation of the bead pack increased as air became randomly distributed throughout the porous medium. The confining column was borosilicate glass which provided for basic visual observations of the bead pack saturation.

In Figure 2 pressure profiles are plotted over the duration of experiments at respective Ca. The pressure gradient during the transient regime followed a chaotic, increasing trajectory. Reaching the steady state regime, the pressure fluctuated around an average differential pressure ΔP. Capillary forces between the competing phases manifest in large fluctuations of ΔP even at lower Ca values. The ΔP fluctuations maintain the same overall magnitude and therefore more pronounced in the low Ca regime when the absolute value of ΔP is lower. Upon stopping the pumps we have $Q = 0$, however, the pressure gradient over the column fell to a non-zero value which we identify as the threshold pressure P_t. We were able to obtain experimental values for P_t that slightly differed between experiments and took the average of these values as a global threshold pressure for the column, $P_t = 5.39$kPa.

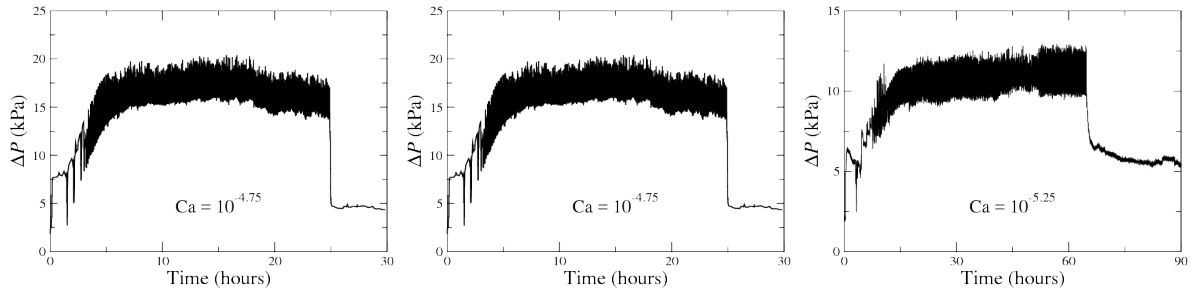

Fig. 2: Three sample pressure plots of the time evolution of the experiment are shown to demonstrate the chaotic and transient nature of the two-phase flow. Plots from the high Ca regime (a), transition point (b), and low Ca regime (c) illustrate the characteristic pressure behavior observed.

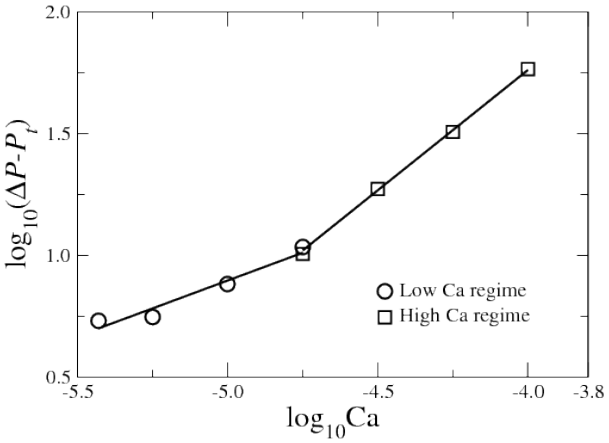

Fig. 3: Plot of excess pressure drop ($\Delta P - P_t$) as a function of the capillary number (Ca) for the nonlinear and linear flow regimes obtained from the experiment. Each data point represents the averaged steady state pressure gradient for the respective Ca. The two scaling exponents for the low and the high Ca regimes obtained from the slopes are 0.46 ± 0.05 and 0.99 ± 0.02 respectively.

As expected, the pressure gradient versus capillary number relationship scaled nearly linearly with $\alpha = 0.99$ for capillary numbers $10^{-4.75}$ and higher. At low capillary numbers, it was shown that the pressure gradient relationship scaled non-linearly with $\alpha = 0.46$. These values support the power scaling theory from Sinha *et al.* and demonstrate that incorporating P_t is crucial to obtain a consistent scaling factor of $\alpha = 0.46$. There was a distinct change from the Newtonian to non-Newtonian flow regime at $\mathrm{Ca} = 10^{-4.75}$. This transition point was far from the value found by similar experimental and numerical studies performed in two-dimensions [5,8].

During initial experimental runs, we observed an ageing effect in our porous medium. The magnitude of ΔP required to maintain a specific two-phase flow rate increased if a time span of several weeks elapsed between measurements, yet all data collected within a short time frame would show a scaling of 0.4–0.5 in the low Ca regime, or 0.95–1.05 in the high Ca regime. Some of this was explained initially by biofouling of the inline filter and mesh, which was avoided by adding a small amount of biocide to the flowing fluid. However, in two-phase flow experiments with a Hele-Shaw cell, Aursjø *et al.* observed this ageing effect phenomena and theorized that it was due to wetting effects [13]. Similarly, we hypothesize wetting

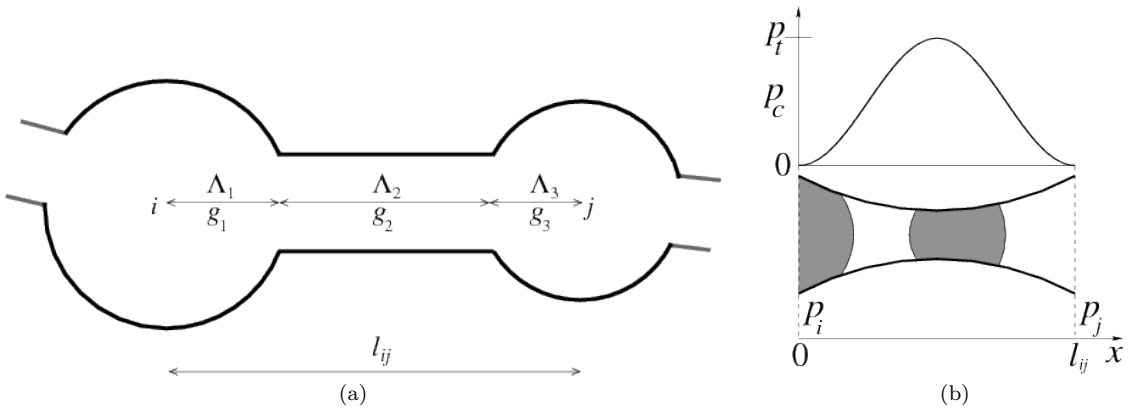

Fig. 4: The schematic of one link between the two nodes i and j is shown in (a). The pore space of each link is divided into three pore-parts, two pore-bodies at two ends and one pore-throat in between. The total length (l_{ij}) of the link is equal to $\Lambda_1 + \Lambda_2 + \Lambda_3$, the sum of each pore-part. The presence of multiple interfaces between the wetting (white) and non-wetting (gray) fluids in a link is shown in the bottom of (b) and the variation of capillary pressure $p_c(x)$ as a function of the interface position (x) for each interface is shown in the top of (b). $p_c = 0$ at the two ends of the link and is maximum, equal to the threshold pressure p_t, at the middle of the tube. $p_t = 4\gamma\cos\theta/r_t$ is the minimum pressure required for the non-wetting fluid to invade the pore.

effects within the column of glass micro-spheres may have contributed to the change of the non-wetting saturation S_{nw}, resulting in a different ΔP for a given two-phase flow rate. This theory is corroborated by the simulations which show ΔP is a function of S_{nw} (see Figure 7). We would like to note that the final data set was performed over the smallest time span possible in order to avoid all ageing effects.

4 Network Model for Two-Phase Flow in Reconstructed Pore Network

Network models of multiphase flow are useful to understand the macroscopic properties of large pore networks relating the underlying pore-scale physics of a porous material [14]. A few decades ago, medical micro-CT (micro computed X-ray tomography) scanners were adopted to scan geological samples [15] and since then there has been a revolution in the new scanning techniques to characterize the micro-structures of porous media [16,17]. To use these pore structures obtained from the 3D images of the pore space as the input to the network models, simplified networks consisting of pores and throats are reconstructed using different approaches. One approach is to use a statistical model [18] where different statistical properties like the porosity distribution, correlation function and linear path function are estimated from the images of 2D thin sections of the sample. Random 3D networks are then generated with the same statistical properties obtained from the images. This method is often questioned and observed to match poorly with the original sample due to the loss of long range geometric connectivity [19,20,21]. Another method of reconstruction is by *process-based* models, where 2D thin section images are analyzed to measure the grain size distribution and other petrophysical properties and then the packing of the grains are simulated following different geological processes, such as sedimentation, compaction, rearrangement and diagenesis [21,22]. These models show good results for samples where sedimentary processes are involved, such as sandstones. However in the case of systems having complex sedimentary and diagenetic history or systems with heterogeneity – such as carbonates – network reconstruction using process based models are difficult.

Network	Physical dimension (mm^3)	Number of nodes	Number of links
A	$1.8 \times 1.8 \times 1.8$	1163	2274
B	$4.5 \times 1.5 \times 1.5$	767	1750
C	$1.0194 \times 1.0194 \times 1.0194$	604	1054

Table 1: Physical dimensions of the porous media samples A, B and C and the number of links and nodes of the corresponding reconstructed networks.

In such cases, to extract the pore networks from any generic 3D image of an arbitrary porous medium, different voxel based models such as medial axis based methods and maximum ball methods are used [23,24]. More details on the different network reconstruction methods can be obtained in the respective references. In the present study we use three different networks reconstructed from (A) Berea sandstone, (B) sandpack and (C) a sandstone ("sandstone 9" in [23]). Networks A and B were reconstructed using the process-based models [21,22] whereas C was reconstructed using a voxel based maximum ball algorithm [23,24]. The physical dimension of the samples A, B and C and the number of links and nodes of the corresponding reconstructed networks are listed in Table 1.

Sample A and B have been used previously e.g. in Ramstad *et al.* [25] and Tørå *et al.* [26] respectively. Samples C is described in [23] and may be found at [27].

The network extracted from a pore sample consists of links that are connected at nodes. The number of links connected to a node is the degree or the coordination number of that node. Each link is associated with a set of parameters which characterize the pore space of the original sample. A link has 3 pore-parts, two pore bodies at the end and one pore throat in between as shown in Figure 4. The cross-section of the pores are triangular in shape and characterized by a shape factor G, defined as the ratio between the effective cross-sectional area of the pore (a) and the square of its circumference. The value of G can vary in the range $(0, \sqrt{3}/36]$ for triangular cross-section where the largest value (≈ 0.048) corresponds to an equilateral triangle. The effective cross-sectional area can then be calculated from the relation $a = r^2/(4G)$, where r is the radius of the inscribed circle in the pore-part [28]. The network transports two immiscible fluids, one is more wetting than the other with respect to the pore wall. We consider that the wetting properties of the fluids are such that there is no film flow in the system and the flow in the pores are piston-like. The instantaneous local flow-rate q_{ij} inside a link between two nodes i and j follows the Washburn equation of capillary flow [29,30],

$$q_{ij} = \frac{g_{ij}}{l_{ij}} \left[p_j - p_i - \sum p_c(x) \right], \tag{3}$$

where p_i and p_j are the local pressure drops at ith and jth nodes. The mobility g_{ij} of the link between the two nodes is calculated from the harmonic average of the individual conductances from each of three pore-parts of that link, given by,

$$\frac{l_{ij}}{g_{ij}} = \frac{\Lambda_1}{g_1} + \frac{\Lambda_2}{g_2} + \frac{\Lambda_3}{g_3}, \tag{4}$$

where $\Lambda_{1,2,3}$ and $g_{1,2,3}$ are the lengths and conductances of each pore-part respectively as shown in Figure 4. For a triangular cross-section, each individual term of $g_{1,2,3}$ for each pore-part of a link is given by [31, 32],

$$g = \frac{3r^2 a}{20\mu_p}, \tag{5}$$

where a and r are respectively the effective area and the radius of the inscribed circle in the pore part. μ_p is the time-dependent saturation-weighted viscosity for the link given by $\mu_p = \mu_{\mathrm{nw}} s + \mu_{\mathrm{w}}(1-s)$, where s is the instantaneous non-wetting saturation inside the link.

The capillary pressure $p_c(x)$ in equation 3 appears due to the surface tension at the interfaces where $x \in [0, l_{ij}]$ is the position of the interface. It acts as a barrier for the non-wetting fluid to penetrate through

the pores filled with the wetting fluid and will be maximum at the narrowest part of the pore, i.e. the pore throat. The pores are in between grains and the links are therefore approximated as hourglass-shaped in the longitudinal direction in terms of the capillary pressure. The functional dependence of the capillary pressure on the interface position inside such a pore is modeled by a modified form of Young Laplace equation [2, 30],

$$|p_c(x)| = \frac{2\gamma\cos\theta}{r_t}\left[1-\cos\left(\frac{2\pi x}{l}\right)\right], \tag{6}$$

where r_t denotes the throat radius which is the narrowest part of the pore. γ is the surface tension and θ is the contact angle between the interface and the pore wall. In our simulations we set $\gamma\cos\theta = 0.03$ N/m. The chosen form of $p_c(x)$ therefore provides the necessary x-dependence so that $p_c(0) = p_c(l) = 0$ and $\max_{x\in[0,l_{ij}]} |p_c(x)| = |p_c(l_{ij}/2)|$. The summation over p_c in equation 3 runs over all the interfaces inside one link.

A constant volumetric flow rate Q is generated through the application of a pressure drop ΔP across the system. Q is of course the same through any cross-section of the network. Local pressures (p_i) at each node are then determined by solving the set of linear equations balancing the flow at each node using the Kirchhoff equations, ensuring that the net flux in any node is zero. This is done by solving the corresponding matrix inversion problem using the conjugate gradient algorithm [33]. When the local node-pressures are known, the local flow rates q_{ij} through each link is calculated using equation 3. This determines the velocity of each interface inside any link. We choose an adaptive time step Δt in such a way that the displacement of any meniscus does not exceed one-tenth of the length of the corresponding link within that time. All the interfaces are moved accordingly which changes the pressure distribution in the network. The pressure at the nodes are then determined again using conjugate gradient algorithm and the whole process is repeated. When an interface reach at the end of a link, wetting and non-wetting bubbles are snapped-off and new interfaces are created in the neighboring links. The rules related to the interface dynamics used in this 3D network model are similar to the 2D network model found in [30,34]. The in- and out-fluxes of the fluids from one node to the neighboring links at any time step is determined from the relative flow-rates of the links connected to that node. As this can increase the number of interfaces in any link infinitely, we put a limit in the maximum number of interfaces inside any link. When this limit is exceeded, we merge the two nearest interfaces keeping the volume of each fluid conserved. In the simulations reported in this article, we have considered a maximum of 4 interfaces in any link.

In order to reach steady state, we need to impose the periodic boundary condition so that the fluid configurations that leave the network from one side can enter from the opposite side and the flow can continue for infinite time. However, the network here is irregular and therefore the two opposite edge surfaces do not match each other which is necessary to apply the periodic boundary condition. We solve this problem by making a mirror copy of the network in the direction of the overall flow and connected the copy with the original network. The edges then match each other and periodic boundary conditions are implemented in the direction of overall pressure gradient. Notice that, this makes the system closed and the fluid saturations do not change with time. The saturation is therefore a control parameter here and we measure the fractional flow, whereas in our experiments we control the fractional flow.

5 Simulation results

Simulations are performed with constant flow rate Q, which sets the capillary number Ca, the ratio of the viscous to the capillary forces at the pore level, given by $\mathrm{Ca} = Q\mu/(\gamma A)$. Here A is the cross-sectional area of the pore space, μ is the saturation weighted viscosity and γ is the surface tension between the two fluids. Here we have considered two viscosity ratios, $M = 1$ where $\mu_{\mathrm{nw}} = \mu_{\mathrm{w}} = 0.1$Pa.s and $M = 0.1$ where $\mu_{\mathrm{nw}} = 10^{-3}$Pa.s and $\mu_{\mathrm{w}} = 10^{-2}$Pa.s. For a reservoir, the oil-water viscosity ratio can vary in a wide

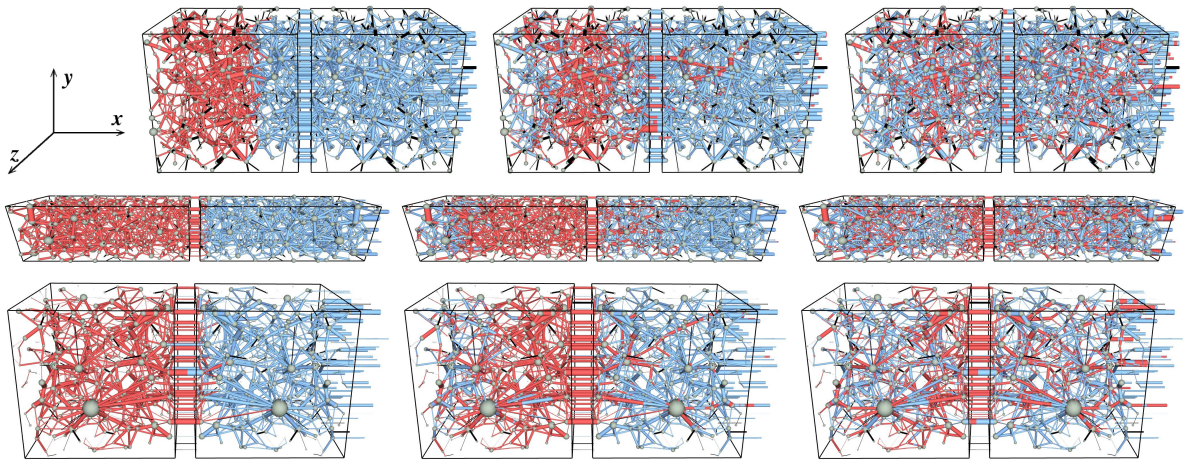

Fig. 5: The time evolution of two-phase flow through the reconstructed networks where the wetting and the non-wetting fluids are colored by blue and red respectively. The few links in black are the dead ends which are connected only at one node and therefore removed from the network. The three images from left to right in each row respectively correspond to the initial condition of the system and after 0.1 and 0.3 pore volumes of fluids have passed. The three rows from top to bottom correspond to the samples A (berea), B (sandpack) and C (sandstone) respectively. The overall flow is in the positive x direction. The periodic boundary condition is implemented in the same direction, by making a mirror image of the original reconstructed network and then connected together with the original. These two parts are shown by the two cuboids in the figures. Here, the system is initialized by filling the links with non-wetting fluid from $x = 0$ until the required saturation is obtained and then filling the rest with the wetting fluid. In these figures, the non-wetting saturations are 0.3 for sample A and 0.5 for B and C.

range depending on the type of the oil and the temperature [35]. Initial transients during the simulation at Ca $= 0.01$ and $M = 1$ are shown in Figure 5 where the wetting and non-wetting fluids are colored by blue and red respectively. There is a few links marked by black. These are those links which are connected only with one node and will act as a dead end. The three rows from top to bottom correspond to the three networks A, B and C respectively and the three snapshots from left to right for each network are taken at three different time steps - at the beginning of the simulation and after 0.1 and 0.3 pore-volumes of fluid have passed. The overall flow is in the positive x direction. There are two cuboids in each network, the one inside the left cuboid is the original reconstructed network and in the right one is the mirror copy of that, which is done in order to implement the periodic boundary condition as discussed earlier. We prepared the initial system by filling it sequentially by two fluids with necessary saturation so that the network is segregated into one part of non-wetting (red) fluid and one part of wetting (blue) fluid as shown in Figure 5. Here $S_{\mathrm{nw}} = 0.3$ for A and 0.5 for B and C. When the simulation starts, the non-wetting fluid starts invading the wetting fluid and depending on the capillary number and viscosity ratio it will either start viscous fingering for high Ca or the capillary fingering when the capillary forces dominate. On the other hand, the wetting fluid also enters the system from left due to the periodic boundary and pushes the non-wetting fluid. This displacement of wetting fluid into the non-wetting is favorable and the displacement should be piston-like or stable displacement. Though the network is small here, one can still observe some signatures of these two different types of fluid displacements in the initial transients – in the right part there are capillary fingers of the red fluid into the blue whereas in the left the blue fluid displaces the red

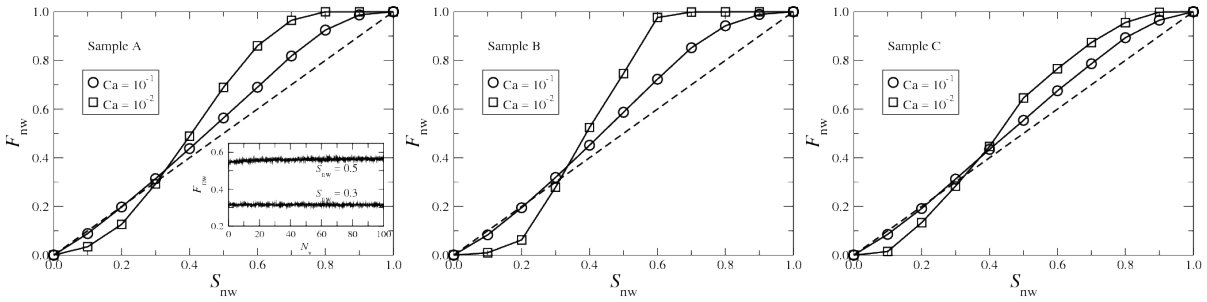

Fig. 6: Plots of non-wetting fractional flow ($F_{\rm nw}$) in the steady state as a function of non-wetting saturation ($S_{\rm nw}$) for the three different networks. The dashed diagonal straight lines correspond to $F_{\rm nw} = S_{\rm nw}$, a system of miscible fluids will follow that line. The results for two different capillary numbers, Ca $= 10^{-1}$ and 10^{-2}, are shown. Notice that the curves approach the diagonal straight line for the higher value of Ca. In the inset for sample A, we plot the fractional flow as a function of pore-volumes ($N_{\rm v}$) of fluids passed, where $F_{\rm nw}$ fluctuates around an average value in the steady-state.

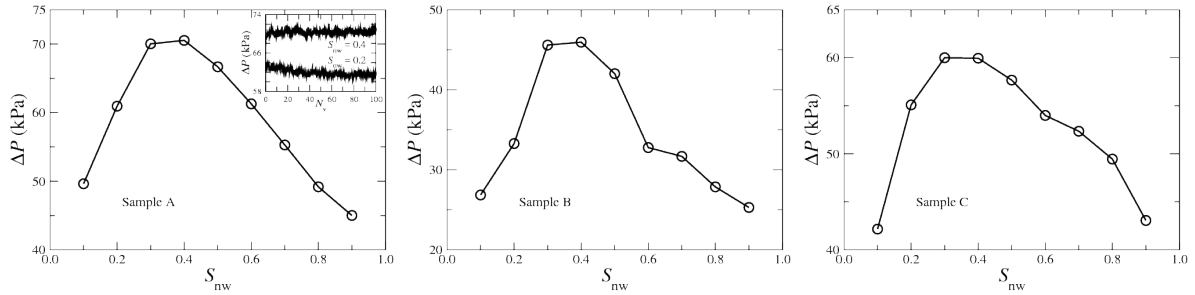

Fig. 7: Total pressure drop (ΔP) in the steady-state for the three networks as a function of $S_{\rm nw}$. The capillary number Ca $= 10^{-2}$. ΔP reaches a maximum at an intermediate saturation, which is due to the increasing number of interfaces causing higher capillary barriers. In the inset of sample A, ΔP is plotted as a function of the pore volumes of fluids passed, which shows the evolution of steady state.

more uniformly with compact propagating front. (More detailed time evolutions of the fluid displacements are presented in the animations in the supplementary material.)

The two fronts catch up with each other with time and the system eventually contains a mixture of two fluids in the steady state. In the steady state, both drainage and imbibition take place at the pore level and fluid clusters are created, merged and broken up. We identify the steady state when the average of any measurable macroscopic quantity stops drifting with time and starts fluctuating around a constant average value. Instead of the sequential initial condition where the two fluids are segregated at two parts of the system, we may start the simulation from a initial condition where the two fluids are distributed randomly. In this case the system reaches to the steady state much faster. Therefore in order to save the computational time we adopted the random initial condition in all the following results. When the system evolves into the steady state, we measure the macroscopic properties with time and take averages of the measurements.

First we present some fundamental properties of the system by measuring the non-wetting fractional flow ($F_{\rm nw}$) and the pressure drop across the system (ΔP) as a function of the saturation. The non-wetting fractional flow is defined as the proportion of non-wetting fluid flowing across the system given by $F_{\rm nw} =$

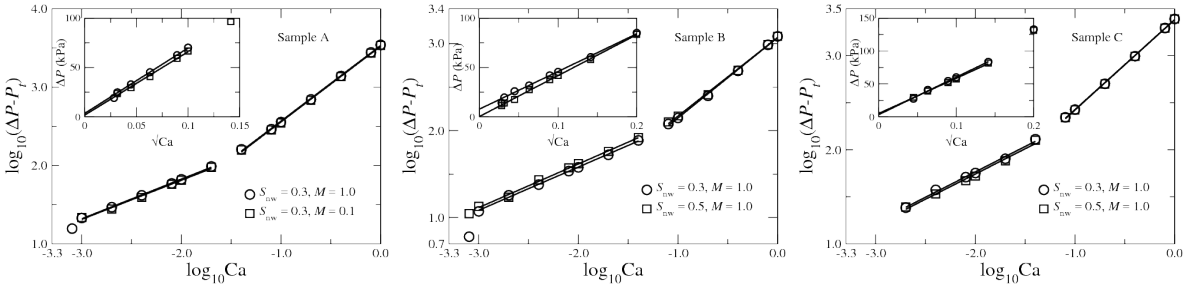

Fig. 8: Plot of overall pressure drop as a function of the capillary number in the steady state for different networks. For network A, results are shown for $S_{\rm nw} = 0.3$ with two different viscosity ratios $M = 1.0$ and 0.1. For B and C, two different saturations $S_{\rm nw} = 0.3$ and 0.5 with $M = 1.0$ are considered. Measurements of the threshold pressures for each simulation are shown in the insets of each figure, where P_t is obtained from the y-axis intercepts of ΔP vs $\sqrt{\rm Ca}$ plots. Using the values of P_t, the scaling exponents are then obtained from the slopes of log-log plots of $(\Delta P - P_t)$ vs Ca.

$Q_{\rm nw}/Q$ where $Q_{\rm nw}$ is the volumetric flow rate of non-wetting fluid through any network cross-section perpendicular to the overall flow. For a set of miscible fluids with no capillary forces, $F_{\rm nw}$ will be exactly equal to $S_{\rm nw}$ in the steady state for any saturation, which is not the case here. The measurements of $F_{\rm nw}$ in the steady state are illustrated in Figure 6. In the inset of the first plot, we show the variation of $F_{\rm nw}$ as a function of the pore-volumes of fluids passed through the system which ensures the steady-state flow situation. The time-averages of $F_{\rm nw}$ in the steady state for the whole range of non-wetting saturation are then plotted for the three different networks at two capillary numbers $\rm Ca = 10^{-1}$ and 10^{-2}. The plots show the well known S-shape and do not follow the diagonal dashed line corresponding to $F_{\rm nw} = S_{\rm nw}$. This is due to the presence of capillary forces at the interfaces for which the two immiscible fluids do not flow equally. The one with the higher saturation dominates the flow, $F_{\rm nw}$ is less than $S_{\rm nw}$ for low values of $S_{\rm nw}$ and higher than $S_{\rm nw}$ for higher values of $S_{\rm nw}$. The curves therefore cross the $F_{\rm nw} = S_{\rm nw}$ line at some point, which is not at $S_{\rm nw} = 0.5$. This shows the asymmetry between the two fluids, as one fluid is more wetting than the other with respect to the pore walls. Moreover, a lower capillary number corresponds to stronger capillary forces relative to the viscous forces and hence the deviation of the curves from the diagonal straight line is higher for $\rm Ca = 10^{-2}$ than for 10^{-1} for each network.

Variation of the global pressure drop ΔP as a function of the saturation $S_{\rm nw}$ for constant overall flow rate (Q) is shown in Figure 7 for the three networks. Here, the capillary number $\rm Ca = 10^{-2}$ for these plots. The initiation of the steady state is illustrated in the inset of sample A, where ΔP fluctuates around an average value in the steady state. The average of ΔP in the steady state first increases with the saturation, reaches a maximum and then decreases again. When $S_{\rm nw}$ is increased from zero, the single phase flow regime, more interfaces start appearing into the system. This increases the overall capillary barrier and to keep the same flow rate (Q) the pressure drop across the system needs to be increased. ΔP is maximum at some intermediate saturation and then starts decreasing again as $S_{\rm nw}$ approaches to 1, as the system again approaches to the single phase flow regime. Interestingly, the maximum of ΔP is not at $S_{\rm nw} = 0.5$, but close to the saturation where $F_{\rm nw}$ crosses the diagonal $F_{\rm nw} = S_{\rm nw}$ line as observed in Figure 6. This was predicted in [36].

We now present the simulation results related to the scaling of ΔP with Q in the steady-state. The values of Ca range from $\approx 10^{-3}$ to 1 in our simulations. We observed that the crossover from the non-linear to the linear scaling falls in this range and we can see both the scaling regimes. We therefore have not performed simulations around $\rm Ca = 10^{-5}$ as we did in our experiments. Results are illustrated in Figure 8 where we plot $\log(\Delta P - P_t)$ as a function of $\log \rm Ca$. First, we need to find the threshold pressure P_t for each

Sample	M	S_{nw}	P_t (kPa)	α (Low Ca)	α (High Ca)
A	1.0	0.3	3.543	0.51 ± 0.01	0.96 ± 0.01
	0.1	0.3	1.745	0.50 ± 0.02	0.97 ± 0.01
B	1.0	0.3	7.795	0.50 ± 0.01	0.92 ± 0.02
	1.0	0.5	0.343	0.50 ± 0.01	0.90 ± 0.02
C	1.0	0.3	3.354	0.54 ± 0.02	0.96 ± 0.01
	1.0	0.5	5.183	0.54 ± 0.03	0.96 ± 0.01

Table 2: Values the threshold pressures P_t and the corresponding scaling exponents α for different simulations. The threshold pressures are obtained from the intercepts in the y-axis of ΔP vs $\sqrt{\mathrm{Ca}}$ plots as shown in the insets of Figure 8. Using the values of P_t, the scaling exponents are then obtained from the slopes of $\log(\Delta P - P_t)$ vs $\log \mathrm{Ca}$ plots.

case. In our experiments, P_t was found by measuring the differential pressure at $Q = 0$. In the simulations for the Bingham fluid [10], P_t was determined by decreasing the external current (or flow-rate) from a large value and identifying the flow-paths with a search algorithm. This procedure is not feasible for dynamic two-phase flow network models, as the interfaces move with time and consequently the flow-paths change. In the case of the two-phase flow simulations in a 2D regular network [8], P_t was measured by minimizing the linear least-square fit errors of $\log(\Delta P - P_t)$ versus $\log \mathrm{Ca}$ data. There, the numerical results were averaged over different samples and time, whereas in the case of the reconstructed 3D network we only have one network per sample and do not have opportunity to do sample averaging. This leads to higher statistical fluctuations in the error measurement and therefore finding P_t based on the minimum error was not possible. Therefore, as P_t is the value of ΔP as $Q \to 0$, we calculated P_t directly from the numerical data of ΔP versus Q. For the low Ca regime, we expect $Q \sim (\Delta P - P_t)^2$ and therefore we plot ΔP as a function of $\sqrt{\mathrm{Ca}}$ which leads to straight lines for the low Ca regime for each sample. The plots are shown in the insets of each plot in Figure 8. Values of the intercepts of the straight lines in the y-axis corresponds the threshold pressure P_t. Using these values of P_t we plot $\log(\Delta P - P_t)$ as a function of $\log \mathrm{Ca}$ in Figure 8 for the three samples for different values of S_{nw} and different viscosity ratios. From the slopes, we see two distinct regimes of flow with two different slopes and there is a sharp crossover in between the two regimes. The results are summarized in in Table 2. For the low Ca regime all the slopes are close to 0.5 which lead to $Q \sim (\Delta P - P_t)^2$ as shown in equation 2. For the high flow rates, all the slopes are close to 1 and the flow is Newtonian.

An interesting aspect we observe concerns the transition point from the nonlinear low-Ca regime to the linear high-Ca regime. This transition point seems to vary between studies. In the experiments, we find it around $\mathrm{Ca} \approx 10^{-4.75}$ while our simulations show it around $\mathrm{Ca} \approx 10^{-1.5}$. Even in the simulations, the transition point seems to vary slightly among different porous media samples A, B, and C. Furthermore, Tallakstad *et al.* did not observe the transition for $\mathrm{Ca} < 10^{-1}$ and therefore it should be at a more higher value [5]. It seems that the transition point is strongly determined by geometric and physical characteristics of the porous medium itself. At this point, we cannot answer how this transition point depends on the network characteristics, saturation or viscosity ratio and will be an interesting aspect to explore in the future.

6 Conclusions

In this article, we presented our experimental and numerical study to investigate the relationship between the pressure drop and the volumetric flow rate in the steady-state two-phase flow of immiscible fluids in three dimensional porous media. Our two-phase flow experiments utilize a three-dimensional porous medium made of glass beads with air and de-ionized water flowing through it. We performed numerical simulations constructing a network model of two-phase flow in 3D reconstructed pore networks. We have

addressed the different nonlinear relationships that were observed in 2D [5] and 3D [7] experiments and in 2D simulations [8] reported earlier. With our experiments and simulations, we show that the capillary pressures at the interfaces in between the immiscible fluids introduce a pressure barrier at each pore and the presence of these barriers in the disorder pore-network effectively creates a yield threshold in the system, making the fluids to behave like a Bingham viscoplastic fluid in a network [10,12,11]. There are two regimes of the flow, in the regime where the capillary forces are comparable with the viscous forces, the flow rate varies quadratically with the excess pressure drop. With the increase in the flow-rate, the capillary pressures become negligible and there is a crossover into a linear flow regime. Both these two flow regimes are well demonstrated by our experiments and simulations in 3D. Our results here in 3D are also in the agreement with the mean-field theory presented earlier [8] which shows that the quadratic scaling does not depend on the dimensionality of the pore network.

We have considered $S_{\rm nw} = 0.3$ and 0.5 in the simulations and $F_{\rm nw} = 0.5$ in the experiments which are in the intermediate range of saturation or fractional flow. In this regime, both the fluids contribute to the flow and a large number of interfaces exist in the system introducing capillary barriers at each pore. If one moves towards $S_{\rm nw} \to 0$ or 1, the system will drift to the single-phase flow regime and eventually the interfaces as well as the capillary barriers will disappear. This should drive the system completely into the linear Newtonian flow regime. The quadratic flow regime we have seen here should therefore disappear as $S_{\rm nw} \to 0$ or 1 and the linear flow regime will cover the whole range of Ca. It will be interesting to study this transition as a function of the saturation or the fractional flow by exploring the whole parameter space. However this needs an enormous range of experiments and simulations as approaching steady state needs many pore volumes of the fluid to be reached. Recently, a Monte Carlo (MC) algorithm has been proposed for the network models of two-phase flow in 2D networks [37] and we look forward towards further development of the MC algorithm for the 3D networks in order to have an efficient way to study the effective scaling of the pressure and the flow rate of steady-state two-phase flow for the whole parameter space in the future.

Acknowledgements We thank Eirik Grude Flekkøy, Knut Jørgen Måløy, Laurent Talon, Signe Kjelstrup, Dick Bedeaux and Morten Vassvik for many interesting discussions. C. Prather, J. Bray, L. Thrane and S. Codd acknowledges support by the National Science Foundation under CBET grant 1335534. A. Bender and M. Danczyk acknowledge support from the Undergraduate Scholars Program at Montana State University. K. Keepseagle acknowledges support from the McNairs Program and from Grant Number P20 RR-16455 from the National Center for Research Resources (NCRR), a component of the National Institutes of Health (NIH). A. Hansen thanks the Beijing Computational Science Research Center and its director, Professor Hai-Qing Lin, for financial support and for providing an excellent atmosphere for doing science.

References

1. J. Bear, *Dynamics of Fluids in Porous Media*, (American Elsevier Pub, New York, 1972).
2. F. A. L. Dullien, *Porous media: Fluid, transport and pore structure*, (Academic Press, San Diego, 1992).
3. H. Darcy, 647 (Les Fontaines Publiques de la Ville de Dijon , Dalmont, Paris, 1856).
4. S. Whitaker, *Flow in porous media I: A theoretical derivation of Darcy's law*, Transp. Porous Med. **1**, 3 (1986).
5. K. T. Tallakstad, H. A. Knudsen, T. Ramstad, G. Lovoll, K. J. Måløy, R. Toussaint and E. G. Flekkøy, *Steady-state two-phase flow in porous media: Statistics and transport properties*, Phys. Rev. Lett. **102**, 074502 (2009).
6. K. T. Tallakstad, G. Løvoll, H. A. Knudsen, T. Ramstad, E. G. Flekkøy and K. J. Måløy, *Steady-state, simultaneous two-phase flow in porous media: An experimental study*, Phys. Rev. E **80**, 036308 (2009).
7. E. M. Rassi, S. L. Codd and J. D. Seymour, *Nuclear magnetic resonance characterization of the stationary dynamics of partially saturated media during steady-state infiltration flow*, New J. Phys. **13**, 015007 (2011).
8. S. Sinha and A. Hansen, *Effective rheology of immiscible two-phase flow in porous media*, Europhys. Lett. **99**, 44004 (2012).
9. S. Sinha, A. Hansen, D. Bedeaux and S. Kjelstrup, *Effective rheology of bubbles moving in a capillary tube*, Phys. Rev. E **87**, 025001 (2013).
10. S. Roux and H. J. Herrmann, *Disorder-induced nonlinear conductivity*, Europhys. Lett. **4**, 1227 (1987).
11. T. Chevalier and L. Talon, *Generalization of Darcys law for Bingham fluids in porous media: From flow-field statistics to the flow-rate regimes*, Phys. Rev. E **91**, 023011 (2015).

12. L. Talon, H. Auradou and A. Hansen, *Effective rheology of Bingham fluids in a rough channel*, Front. Phys. **2**, 24 (2014).
13. O. Aursjø, M. Erpelding, K. T. Tallakstad, E. G. Flekkøy, A. Hansen and K. J. Måløy, *Film flow dominated simultaneous flow of two viscous incompressible fluids through a porous medium*, Front. Phys. **2**, 63 (2014).
14. V. J. Niasar and S. M. Hassanizadeh, *Analysis of fundamentals of two-phase flow in porous media using dynamic pore-network models: A review*, Critical Rev. Env. Sc. Tech. **42**, 1895 (2012).
15. T. Hurst, *CT scannersfrom the hospital to the oil field*, Quest (Bellaire Research Center, Shell Oil Company, Houston) **12**, Cover3 (1984).
16. J. H. Dunsmoir, S. R. Ferguson, K. L. D'Amico and J. P. Stokes, *X-ray microtomography: a new tool for the characterization of porous media*, Proceedings of the Annual Technical Conference and Exhibition **SPE-22860-MS**, (1991).
17. M. J. Blunt, B. Bijeljic, H. Dong, O. Gharbi, S. Iglauer, P. Mostaghimi, A. Paluszny and C. Pentland, *Pore-scale imaging and modeling*, Adv. Wat. Res. **51**, 197 (2013).
18. H. Okabe and M. J. Blunt, *Pore space reconstruction using multiple-point statistics*, J. Petro. Sc. Eng. **46**, 121 (2005).
19. C. Manwart, S. Torquato and R. Hilfer, *Stochastic reconstruction of sandstones*, Phys. Rev. E **62**, 893 (2000).
20. Y. Jiao, F. H. Stillinger and S. Torquato, *A superior descriptor of random textures and its predictive capacity*, Proc. Natl. Acad. Sci. U.S.A. **106**, 17634 (2009).
21. P-E. Øren and S. Bakke, *Process Based Reconstruction of Sandstones and Prediction of Transport Properties*, Transp. Porous Med. **46**, 311 (2002).
22. P-E. Øren and S. Bakke, *Reconstruction of berea sandstone and pore-scale modelling of wettability effects*, J. Petro. Sc. Eng. **39**, 177 (2003).
23. H. Dong, *Micro-CT imaging and pore network extraction*, PhD Thesis, Imperial College London (2007).
24. H. Dong and M. J. Blunt, *Pore-network extraction from micro-computerized-tomography images*, Phys. Rev. E **80**, 036307 (2009).
25. T. Ramstad, A. Hansen and P. E. Øren, *Flux-dependent percolation transition in immiscible two-phase flow in porous media,* Phys. Rev. E, **79**, 036310 (2009).
26. G. Tørå, P-E. Øren and A. Hansen, *A dynamic network model for two-phase flow in porous media*, Transp. Porous Med. **92**, 145 (2012).
27. www.imperial.ac.uk/earth-science/research/research-groups/perm/research/pore-scale-modelling/micro-ct-images-and-networks/sandstone-s9/.
28. G. Mason and N. R. Morrow, *Capillary behavior of a perfectly wetting liquid in irregular triangular tubes*, Journal of Colloid and Interface Science **141**, 262 (1991).
29. E, W. Washburn, *The dynamics of capillary flow*, Phys. Rev. **17**, 273 (1921).
30. E. Aker, K. J. Måløy, A. Hansen and G. G. Batrouni, *A two-dimensional network simulator for two-phase flow in porous media*, Transp. Porous Med. **32**, 163 (1998).
31. W. E. Langglois, *Slow Viscous Flow*, (The Macmillan Company, New York, 1964).
32. P. Jia, M. Dong, L. Dai and J. Yao, *Slow viscous flow through arbitrary triangular tubes and its application in modelling porous media flows*, Transp. Porous Med. **74**, 153 (2008).
33. G. G. Batrouni and A. Hansen, *Fourier acceleration of iterative processes in disordered systems*, J. Stat. Phys. **52**, 747 (1988).
34. H. A. Knudsen, E. Aker and Alex Hansen, *Bulk flow regimes and fractional flow in 2D porous media by numerical simulations*, Transp. Porous Med. **47**, 99 (2002).
35. J. L. M. Barillas, T. V. Dutra Jr. and W. Mata, *Improved oil recovery process for heavy oil: A review*, Brazilian J. Petro. Gas **2**, 45 (2008).
36. A. Hansen, S. Sinha, D. Bedeaux, S. Kjelstrup, I. Savani and M. Vassvik, *A new set of equations describing immiscible two-phase flow in porous media,* submitted to Transp. Porous Med.
37. I. Savani, S. Sinha, A. Hansen, D. Bedeaux, S. Kjelstrup and M. Vassvik, *A Monte Carlo algorithm for immiscible two-phase flow in porous media*, to appear in Transp. Porous Med., (2016).